Grid Generated Turbulence for an Aeroacoustic Facility

Luke Bowen*, Alper Celik†, Mahdi Azarpeyvand‡
Faculty of Engineering, University of Bristol, BS8 1TR, UK

Carlos R. Ilário da Silva§
Embraer, Sáo José dos Campos, 12227-901, Brazil

This paper provides an insight into the grid generated turbulence for aeroacoustic studies. Several passive grids of square bars were tested in the open-jet aeroacoustic facility at the University of Bristol. The geometric properties of the grids and their position within the tunnel contraction nozzle were varied to quantify their influence on the average and statistical flow properties, as well as the generated self-noise. Moreover, case studies involving turbulence interaction noise generation with a NACA0012 airfoil and cylinder were conducted. Turbulence intensity, integral length scale, and the anisotropy of the flow generated by each grid were characterized by hot-wire measurements, and the associated far-field noise was measured by a far-field microphone array. The grid turbulence results show that the downstream evolution of the turbulence intensity and integral length scale was comparable to results of closed test-section wind tunnel studies for the first hydraulic diameter downstream of the contraction nozzle exit. However, beyond the first hydraulic diameter, the turbulence intensity plateaus and the integral length scales show a rapid growth. Moreover, the results show that grids positioned closest to the contraction nozzle exit produced turbulence closest to isotropy with high levels of turbulence intensity, but the measured noise spectra suffered from the contamination from the grids self-noise. The grids located furthest from the contraction nozzle exit performed best in terms of noise contamination and could generate almost the same level of turbulence properties as the grids closest to the contraction nozzle exit.

I. Nomenclature

a_N = Contraction nozzle height [mm]
a_G = Grid height [mm]
b_N = Contraction nozzle width [mm]
b_G = Grid width [mm]

*Ph.D Student, Department of Mechanical Engineering, luke.bowen@bristol.ac.uk
†Postdoctoral Research Associate, Department of Mechanical Engineering, alper.celik@bristol.ac.uk
‡Professor of Aerodynamics and Aeroacoustics, Department of Mechanical Engineering, m.azarpeyvand@bristol.ac.uk
§Challenge Owner in Electrifying Aviation, Embraer, Sáo José dos Campos, Brazil, carlos.ilario@embraer.com.br
A preliminary version of this paper was presented at the AIAA Aviation 2020 forum (Paper 2020-2525).

d	=	Bar diameter [mm]
D	=	Cylinder diameter [mm]
D_H	=	Hydraulic diameter [-]
E	=	One-dimensional turbulence energy spectrum [dB/Hz]
f	=	Frequency [Hz]
$K(u_S)$	=	Kurtosis [-]
k_e	=	Wavenumber range of energy-containing eddies [-]
k_x	=	Stream-wise wavenumber [-]
M	=	Mesh size [mm]
$OASPL$	=	Overall sound pressure level [dB]
p	=	Pressure [Pa]
p_{ref}	=	Reference pressure 2 x 10^{-5} [Pa]
PSD	=	Power spectral density [dB/Hz]
R	=	Grid Contraction ratio [-]
R_{uu}	=	Normalized autocorrelation function [-]
St	=	Strouhal number [fD/U_∞]
$S(u_S)$	=	Skewness [-]
t	=	Time [s]
TI	=	Turbulence intensity [-]
U_∞	=	Free-stream velocity [m/s]
u_S	=	Velocity fluctuation (from single wire measurements) [m/s]
U	=	Stream-wise velocity [m/s]
u	=	Stream-wise velocity fluctuation [m/s]
V	=	Crosswise velocity [m/s]
v	=	Crosswise velocity fluctuation [m/s]
W	=	Chordwise velocity [m/s]
w	=	Chordwise velocity fluctuation [m/s]
x_G	=	stream-wise distance between contraction nozzle and grid location [mm]
β	=	Anisotropy level [-]
Γ	=	Gamma function [-]
θ	=	Polar angle of microphone to flow direction [°]
Λ_x	=	Integral length scale [mm]
λ	=	Dissipation length scale [mm]
ν	=	Kinematic viscosity [m^2s^{-1}]
σ	=	Grid solidity ratio [-]
τ	=	Time-delay [s]
ϕ_{pp}	=	Power spectral density of the pressure fluctuation [dB/Hz]
$\phi_{u_S u_S}$	=	Power spectral density of the velocity fluctuation (from single wire measurements) [dB/Hz]

II. Introduction

AERODYNAMIC noise is becoming an ever-increasing environmental problem and has attracted considerable research interest in recent years. The challenges of noise abatement in the aviation industry continue to gain momentum,

but more sectors are finding environmental consideration of noise an important design constraint. Acoustically treated wind tunnels are essential tools for studying noise mechanisms and understanding the associated flow physics. The full apprehension of the noise generation and radiation mechanisms is being built around extensive testing, which can be employed for validating CFD simulations or improving prediction models. Among other noise sources, turbulence interaction noise has been considered as an important noise generation mechanism due to its relevance with numerous applications such as rotor-stator interaction noise and propeller-pylon interaction noise. Most practical applications can be simplified to a turbulent inflow and a body for the flow to interact with, whether that be a cylinder, an airfoil, or a flat plate. An important challenge for aeroacoustic testing is to achieve direct noise measurements, using free-field microphones which allows for accurate observation of the full sound spectrum using at different observer locations. Such measurements allow for the calculation of important acoustic properties, such as noise directivity and near-field to far-field signal coherence, and also reduce the reliance on more complicated measurement techniques such as phased array systems. To conduct direct noise measurements, an effective method for turbulence generation is required to elevate the radiated noise from the body without significant contamination from the low level of the background noise generated by the flow. The fundamentals of turbulence interaction noise have already had a great deal of interest [1–7], and with the recent influx in studies on passive leading edge treatments for noise reduction, such as serrations [8–15] or porous materials [16–19], turbulence generation for aeroacoustic facilities deserves further study.

Since the inaugural works of Simmonds and Salter [20], passive grid generated turbulence emerged as a highly studied field [20–26]. Although manufacturing and measurement technologies have allowed for more complicated designs of fractal grids [27] and active grids [28] for tailoring turbulence, the design of grids for aerodynamic and aeroacoustic measurements has remained relatively simple. However, there remains a lot of interest in simple passive grids which can produce homogeneous, nearly isotropic turbulence from 10 mesh lengths downstream [21]. To further improve the isotropy, it is generally considered that an axisymmetric contraction ratio of 1.3 from the location of the grid is preferable, to strain the turbulence and to force unity between the three components of the velocity fluctuations [24]. For open-jet aeroacoustic facilities, this becomes a more complex problem, and a balance between the generation of high-quality turbulence and minimisation of self-noise of the grid must be struck. The literature addresses studies that have been performed at facilities with high contraction ratio nozzles, where the grids were located either in the contraction nozzle or at the nozzle outlet. Amiet [1] led the way for turbulence interaction noise study and carried out experiments between a turbulent stream and an airfoil at the UARL facility, where the grid for turbulence generation was located upstream of the contraction nozzle. The presented experimental data had the background noise subtracted, which matched well with the implemented prediction method. The method using a grid that is mounted inside the contraction has been relatively common practise in aeroacoustics, where facility design allows. Moreau *et al*. [6] and Paruchuri *et al*. [29] mounted grids inside the contraction nozzle to reduce grid self-noise and enable direct far-field noise measurement. The high contraction ratio could render the isotropic assumption of the flow questionable. Hutcheson *et al*. [7] and

Geyer *et al.*[18] mounted grids at the contraction nozzle outlet of their respective facilities and conducted turbulence interaction noise experiments. Hutcheson *et al*. [7] utilized acoustic treatments in the form of wedges were attached to the back of the grid to reduce grid noise and prevent Aeolian tones. Geyer *et al.*[18] however, employed the use of a microphone beamforming array to measure the interaction noise, but concluded that turbulence generation for aeroacoustic facilities deserved further study [18]. In an effort to further understand the noise generated by grids and screens, Geyer *et al* [30], conducted a study using a plethora of grids, nets and screens mounted at the contraction nozzle outlet. The study assessed the pressure drop across the screen and related it to the grid self-noise, resulting in a basic prediction tool for the frequency-dependent noise generated by nets or screens.

As discussed above, the contraction ratio between the location of the grid and the outlet of the nozzle is an important consideration for studying turbulence interaction noise. A grid mounted at the contraction nozzle outlet, and subject to the free-stream velocity will likely generate significant self-noise and contaminate any turbulence interaction noise. To reduce the self-noise, placing the grid further inside the contraction nozzle will reduce the local velocity at the grid and thus the grid self-noise. Mounting a grid further inside the contraction nozzle outlet will benefit from improved isotropy up to a contraction ratio of 1.3 [24]. Increasing the contraction ratio beyond 1.3 may cause implications with the quality of the generated turbulence. The contraction amplifies the transverse components of velocity fluctuation, therefore a large contraction may cause the transverse fluctuation to exceed the axial component forcing an anisotropic turbulent flow.

This paper aims to investigate the compromise between the quality of the generated turbulence and the grid self-noise for open-jet aeroacoustic facilities, and to document the effect of grid location within the contraction nozzle to aeroacoustic measurements in open-jet aeroacoustic facilities. The remainder of the manuscript is organised as follows. Section III explains the aeroacoustic facility, the turbulence grids, measurement setup and the techniques used. Section IV presents the results and discussion in two subsections. Section IV.A presents the results on the flow properties, and Sec. IV.B presents the far-field measurements performed for grid self noise studies and case studies. Finally, the paper is completed by Sec. V, where the conclusions of the study are reported.

III. Measurement setup

An extensive experimental study was conducted by employing 12 passive grids of varying geometric parameters to understand the effect of geometric parameters and grid location on the turbulence properties in an aeroacoustic facility. This section details the aeroacoustic facility, the turbulence grids and the measurement techniques employed to enable the analysis of the grid self-noise and to characterise the generated turbulent flow. Case studies involving turbulence interaction with a NACA0012 airfoil and a cylinder were also carried out to assess the performance of the grids in typical experimental applications.

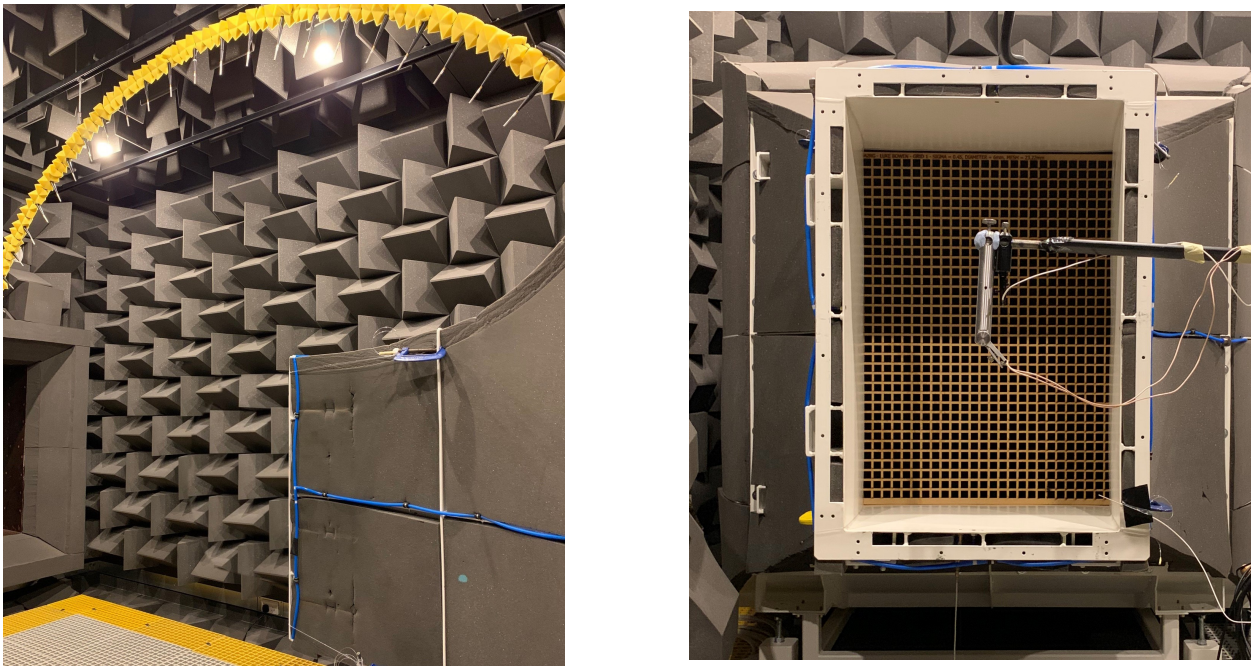

(a) (b)

Fig. 1 Pictures of the facility including (a) the contraction, collector and microphone array and (b) a grid inside the contraction at location A and the CTA hot-wire setup.

A. Wind Tunnel

The experiments were carried out in the University of Bristol Aeroacoustic Facility, which is a closed-circuit, open-jet wind tunnel. The contraction nozzle opens into the anechoic chamber with the dimensions of 6.7 m in length, 4 m in width and 3.3 m in height, and it is anechoic down to 160 Hz [31], see Fig. 1. Figure 2 illustrates a schematic of the contraction nozzle with exit dimensions of a_N = 500 mm and b_N = 775 mm, which allows for steady operation of the anechoic wind tunnel facility for flow velocities from 5 m/s to 45 m/s and a free-stream turbulence intensity below 0.2% [31]. A cartesian coordinate system (x, y, z) is located at the center of the nozzle exit plane to ease the interpretation of the results. The stream-wise direction (x), the vertical direction (y), and the lateral direction (z) are associated with flow components u, v and w, respectively.

B. Turbulence grids

Grid generated turbulence for closed test section wind tunnels is a well-documented research area [21, 22, 24, 25, 27, 28, 32]. However, there is a limited number of studies addressing the turbulence generation in open-jet wind tunnel facilities, specifically in the context of aeroacoustic wind tunnels, where the issue of noise is of paramount importance. The design of the grid geometry can be key to the control of the downstream properties of a fully developed turbulence [22, 23]. In this study, a set of 12 passive grids were placed at three locations upstream of the contraction nozzle exit, which are identified in Table 1 and depicted in Fig. 2. An example of a grid mounted within the contraction is displayed

in Fig. 1b. The grids were manufactured by laser cutting square perforations in to sheets of medium-density fibreboard (MDF) with a thickness of 9 mm. Although grids with various bar profiles have been investigated in the literature, this study was restricted to the square bar grids, which are known to be quieter, as well as generating higher levels of turbulence than round bars [33]. The parameters which define the grids geometry are the mesh size (M), the bar diameter (d), and the grid solidity factor (σ). The grid solidity factor (σ), given by $\sigma = d/M(2 - d/M)$, is the measure of the cross-sectional area of the grid to the total area of the grid. Table 2 lists these geometric parameters of each of the grids used in this study, as illustrated in Fig. 3. Moreover, the location of the grid within the contraction nozzle is an important parameter affecting the grid self-noise. The grid contraction ratio is the area ratio between the grid area, which depends on the location of installment, and the nozzle exit area. The grid contraction ratio, R, is defined as $R = (a_G b_G)/(a_N b_N)$, where a_G and b_G denote the dimensions of the grid, and a_N and b_N denote the dimensions of the nozzle outlet. For aerodynamic purposes, a mesh grid with a contraction ratio of 1.3 is widely documented as the optimum for isotropic homogeneous turbulence generation [24]. However, for the case of turbulence generation in aeroacoustic facilities for direct turbulence interaction noise measurements, the self-noise generated by the grid should be taken into consideration to sustain desired low levels of background noise. Essentially, this study establishes the trade-off between the level of anisotropy of the generated turbulence and the grid self-noise. Figure 2 displays a schematic of the contraction nozzle with the three studied grid locations, A, B, and C, depicted by Figs. 2b, 2c and 2d, corresponding to the grid contraction ratios of $R = 1.3$, $R = 2.4$ and $R = 4.4$, respectively.

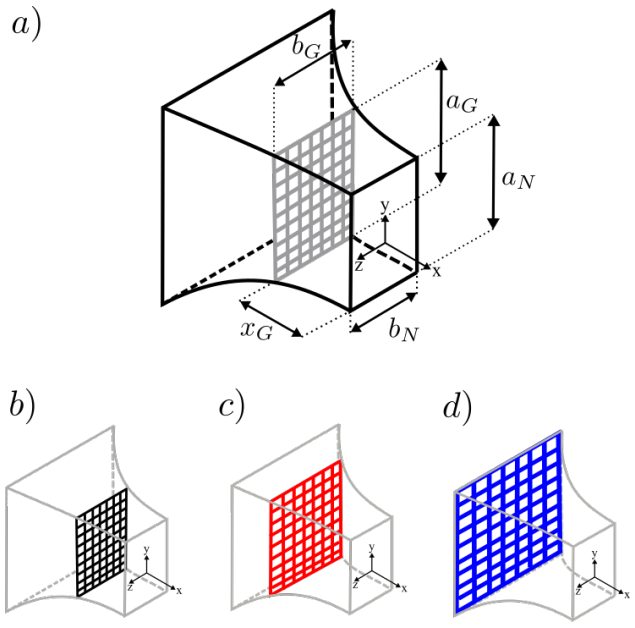

Fig. 2 Schematics of the contraction nozzle with the turbulence grids, (a) the contraction nozzle and the defining geometry definitions, (b) grid location A ($R = 1.3$), (c) grid location B ($R = 2.4$), and (d) grid location C ($R = 4.4$).

Table 1 The geometric properties of test locations in the contraction nozzle.

Grid Location	Height, a_G (mm)	Width, b_G (mm)	x_G (mm)	R
A	838	613	500	1.3
B	1023	911	820	2.4
C	1305	1305	1040	4.4

C. Case studies: Airfoil and cylinder models

In the context of aeroacoustic studies, turbulence interaction noise experiments require elevated levels of turbulence intensity to increase the radiated noise levels, which enable direct noise measurements and provide a consistent data set for analytical models in the literature [1]. This is achieved by generating significantly higher turbulence intensity levels compared to the normal smooth flow of the wind tunnel jet. Two case studies were performed to elucidate the effects of the grid turbulence properties on the aeroacoustic measurements.

A case study was conducted using a NACA 0012 airfoil, and the interaction noise was studied to provide information on the effect of generated turbulence and grid self-noise to turbulence interaction noise measurements. Figure 4a depicts the measurement set-up with the mounted airfoil. The airfoil had a chord length of 0.2 m with a leading edge radius of 3.2 mm and a span of 0.5 m. The airfoil was mounted within side plates, attached to the vertical sides of the contraction nozzle. The distance between the contraction nozzle and leading edge of the airfoil was approximately one hydraulic diameter, i.e., x = 0.65 m. The airfoil was manufactured from Polylactic Acid (PLA) using additive manufacturing technology. The surface of the airfoil was post-processed to improve the surface finish to an approximate surface roughness of 0.1 μm. Although not used in this study with its full capability, the airfoil is well instrumented for both static pressure and unsteady surface pressure measurements. The static pressure measurements were used to validate the NACA 0012 profile against XFoil predictions for a variety of inflow conditions [19].

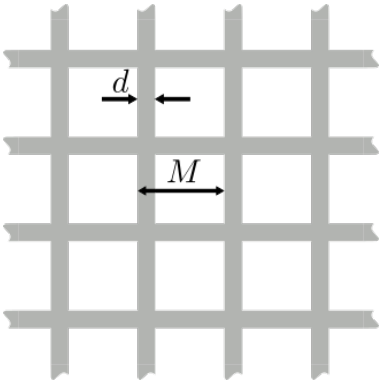

Fig. 3 Geometric definition of the grids.

The second case study to exemplify the effects of the grid generated turbulence on the aeroacoustic measurements was a cylinder-turbulent flow interaction, which has a broad area of applications. The cylinder was made from smooth

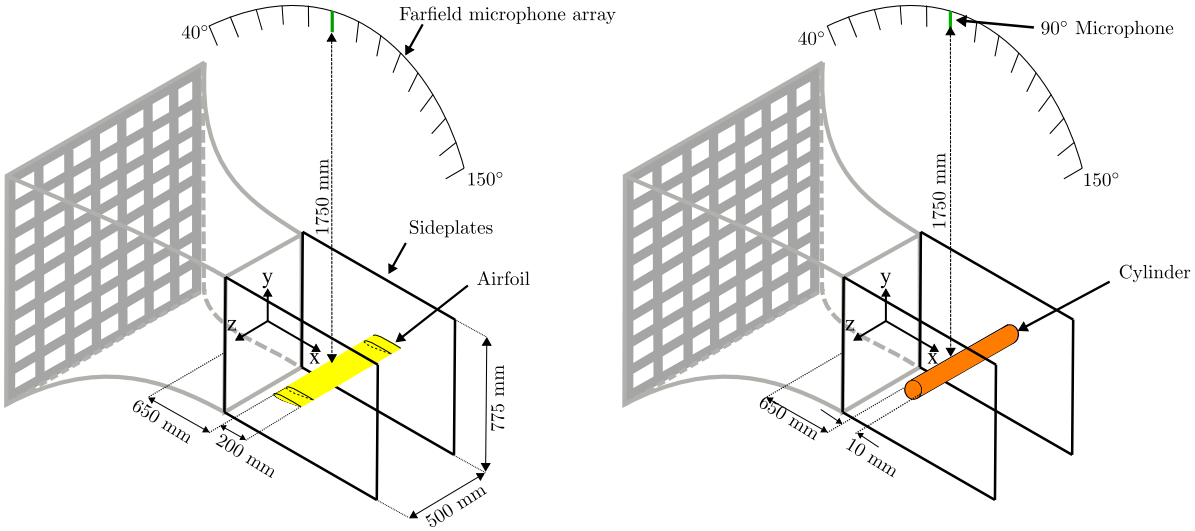

Fig. 4 Schematics of the the contraction nozzle with a representative turbulence grid and the set up of (a) the NACA 0012 airfoil, and (b) a cylinder of 10 mm diameter, both mounted in side plates that is used in the turbulence interaction noise case studies.

aluminium which was 10 mm in diameter and was mounted in the flow using a similar set up to the airfoil model, see Fig. 4b. It was mounted horizontally in the centre of nozzle jet plume at $x = 650$ mm downstream from the nozzle exit i.e. at one hydraulic diameter.

D. Far-field noise measurements

Both the self-noise of the grids and the generated turbulence interaction noise were measured using a far-field microphone array. The array was an arc consisting of 23 microphones arranged in 5° increments between polar angles of 40° and 150°, allowing for detailed directivity measurements. The arc was placed 1.75 m above the center of the wind tunnel jet and the microphone located at 90° to the free-stream was positioned directly above the leading edge of the airfoil. The far-field noise data was measured using 1/4 inch GRAS 40PL free-field microphones, which exhibit a flat frequency response for a large dynamic range of 10 Hz to 10000 Hz, with an uncertainty level of ±0.2 dB after calibration. Each microphone was calibrated prior to the tests using a GRAS 42AA pistonphone calibrator.

E. Hot-wire anemometry setup

The turbulent flow properties were characterized by the use of Constant Temperature Anemometry measurements. A Dantec 55P16 single-wire probe and a two component 55P51 cross hot-wire probe were used in tandem. Both probes were operated using a Dantec Streamline Pro system with a CTA91C10 module, using a National Instruments PXIe-4499 module mounted in a National Instruments PXIe-1026Q chassis for data acquisition. The data was simultaneously sampled from both probes at a rate of 2^{15} Hz for a duration of 8 seconds. Both the single-wire and cross-wire probes

were calibrated using a Dantec 54H10 calibrator. The cross-wire probe was also calibrated for yaw angles between $-40°$ and $40°$. The uncertainty of the free-stream velocity measurements was 5.17% and 2.72% for the minimum and maximum free-stream velocities, 10 m/s and 25 m/s, respectively. The vertical (V) and lateral (W) velocity measurement uncertainties were 12.3% and 11.3% for the lowest value of the corresponding velocity component at a free-stream velocity of 20 m/s, respectively. All uncertainties were calculated using the detailed procedure from Jørgensen [34]. The relatively high uncertainty of the cross-wire measurements is due to the performance of the probe at low velocities, and is consistent with the literature [35, 36] The probes were located symmetrically about the y-axis at the centre of the jet plume core (see Fig. 4a). The probes were initially positioned at $x = 0$, $z = 0$ with the single wire and x-wire at $y = 50$ mm and $y = -50$ mm, respectively. The single-wire probe was used for the measurement of the freestream velocity properties, while the cross-wire probe was employed to measure the individual U, V and W velocity components. The orientation of the cross-wire was aligned to the x-axis to measure streamwise (U) and vertical (V) velocity components and to provide both the streamwise (U) and lateral (W) velocity components the probe was rotated $90°$ about the x-axis. To evaluate the downstream evolution of the turbulence statistics, the probes were traversed along the x-axis between $0 < x/D_H < 1.65$.

IV. Results and Discussion

This section presents the turbulence characteristics of the flow generated by grids and the aeroacoustic performance of the grids in terms of self-noise generation and their employability for turbulence interaction noise studies. First, the turbulence properties of the flows, generated by grids under investigation, are evaluated. This is achieved by characterizing the flow properties, and presenting the results of turbulence intensity, integral length scale and anisotropy. Secondly, the results of the far-field noise measurements are presented. The far-field noise measurement results include an evaluation of the self-noise generation for all the grids under investigation and the results of the turbulence interaction case studies. Both sections present results for a mean flow velocity of $U_\infty = 20$ m/s. Based on previous studies, the presented distance downstream is non-dimensionalized by mesh length [21, 22]. However, for aeroacoustic studies in open-jet anechoic wind tunnels, test rigs are typically mounted within one hydraulic diameter of the nozzle to avoid effects from shear layers and to stay within the potential core of the jet. For this reason, in this study the distance from the nozzle exit is non-dimensionalized by the hydraulic diameter, with the coordinate system (x, y, z) set to the center of the contraction nozzle exit, as shown in Fig. 4. The nozzle hydraulic diameter is defined by $D_H = (2a_N b_N)/(a_N + b_N)$, where a_N and b_N are the height and the width of the nozzle exit, as illustrated in Fig. 2. The results are presented according to the three grid locations within the contraction nozzle, A, B and C, which are defined by Fig. 2. Recall that at locations A, B and C, the contraction ratios are $R = 1.3,\ 2.4$ and $R = 4.4$, respectively. Moreover, at each location four different grids were investigated, whose geometric properties and the associated flow features are presented in Table 2.

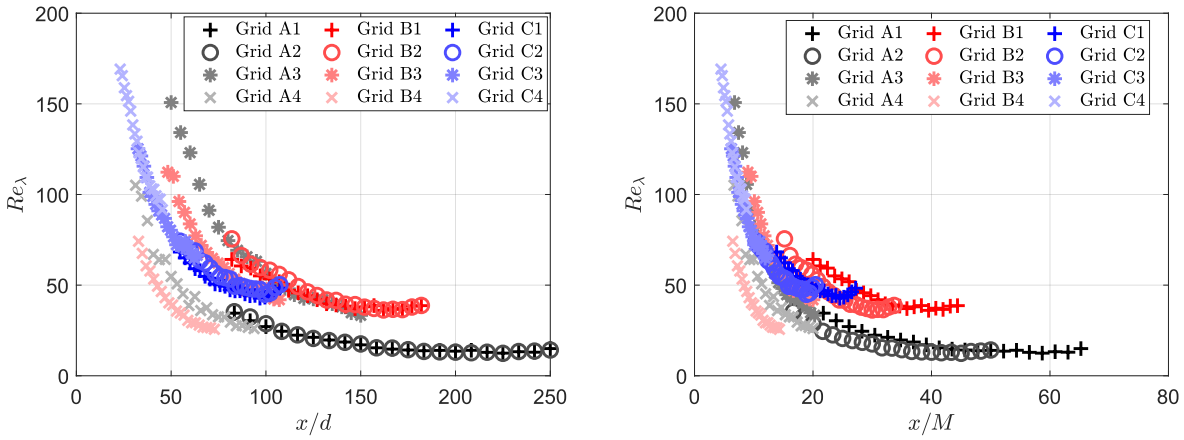

Fig. 5 Downstream evolution of Taylor Reynolds number for (a) downstream distance non-dimensionalized by grid diameter (x/d) and for (b) downstream distance non-dimensionalized by grid mesh size (x/M).

A. Flow properties

This section provides a detailed analysis of the turbulent flow properties generated by grids employed in this investigation. Results are presented for the turbulence intensity, the integral length scale of the turbulent structures, and the anisotropy of the turbulence. The downstream evolution of these quantities starting from the nozzle exit is also addressed in the discussions. Although not presented in the paper, the flow homogeneity was assessed and the results demonstrated almost uniform values within $y = \pm 300$ mm and $z = \pm 200$ mm of the centre of the potential core of the wind tunnel jet.

Figure 5 presents the results of the downstream evolution of Taylor Reynolds number, $Re_\lambda = u'\lambda/\nu$, where u' is the root-mean-square of velocity fluctuation, λ is the Taylor microscale and ν is the kinematic viscosity of air at room temperature. The downstream evolution of Re_λ along the measured domain is non-dimensionalized by grid diameter, d (Fig.5a), and mesh size M (Fig.5b). Generally, the grids exhibit a range of Re_λ values which appear to be greatest, closest to the grid and the greatest decay rates are observed within $0 < M < 20$. Grids that generate higher turbulence intensities generate larger Taylor Reynolds numbers, and grids that possess common bar diameter exhibit comparable Re_λ values. The results of most grids lie approximately on the same curve when the downstream distance is non-dimensionalized by M, with the exception of B1 and B4.

1. Turbulence Intensity

This section presents the results of turbulence intensity (TI) generated by different grids and the downstream evolution of the turbulent flow generated. Since the level of radiated noise from a body immersed in a flow is directly related to the level of turbulence intensity of the flow, it is essential to properly study this quantity for each grid. To do so, a detailed analysis was performed on the time-series data obtained by hot-wire measurements. The geometric

properties of each grid and the associated turbulence intensities are presented in Table 2 for a free-stream velocity of 20 m/s. Table 2 also presents the values of the integral length scales, which will be discussed later in Section IV.A.2 The turbulence intensity can be defined as,

$$TI = \frac{1}{U_\infty}\sqrt{\frac{1}{3}(u'^2 + v'^2 + w'^2)}, \tag{1}$$

where the root-mean-square of the velocity fluctuation in the stream-wise direction (x), the vertical direction (y), and the lateral direction (z), are represented by u', v' and w', respectively.

Table 2 The geometric properties and identification of each turbulence grid, turbulence intensity and integral length values estimated by the autocorrelation method at the position contraction nozzle exit ($x = 0$), at a free-stream velocity $U_\infty = 20m/s$.

Grid	Diameter, d (mm)	Mesh, M (mm)	σ	Turbulence intensity (%)	Integral length scale (mm)
$A-1$	6	23	0.45	4.3	4.5
$A-2$	6	30	0.35	4.9	5.3
$A-3$	10	74	0.25	8.9	8.5
$A-4$	16	85	0.40	12.8	9.6
$B-1$	10	41	0.45	4.5	5.6
$B-2$	10	54	0.35	4.8	5.8
$B-3$	17	91	0.35	7.0	7.1
$B-4$	25	127	0.35	8.9	6.4
$C-1$	19	75	0.45	4.8	5.9
$C-2$	19	100	0.35	4.9	6.1
$C-3$	32	167	0.35	8.1	9.4
$C-4$	45	233	0.35	10.1	10.8

Figure 6 presents the downstream evolution of the total turbulence intensity accounting for u, v and w, as per Eq. 1, for the distance $0 < x/D_H < 1.65$ in the grid generated flows. The results are grouped and presented by their location in the contraction nozzle. Figures 6a to 6c demonstrate the results for grid contraction ratios from $R = 1.3$ to $R = 4.4$, respectively. It is evident that all the grids generate a level of turbulence intensity higher than the wind tunnel jet without the grid, i.e., $< 0.2\%$ [31]. The lowest and highest value of the generated turbulence intensity of all the grids at the contraction nozzle outlet ($x/D_H = 0$) is 4.2% and 12.8%, and is generated by grids A1 and A4, respectively. Moreover, the highest turbulence intensity levels at $x/D_H = 1$ are generated by the grids installed at location C. The high levels of turbulence intensity far downstream of the nozzle exit exhibited by grids at location C may be attributed to the bar diameter, d. The values of d for the grids installed at location C are significantly larger than the corresponding values for grids at location B, with a comparatively small variation in x_G ($220mm$). At $x/D_H = 1$, the highest level of turbulence intensity is generated by grid C4 with a value of 7.8%.

The decay trend of the turbulence intensity along the measurement axis is also of worth noting, and exhibits some interesting behaviours. The decay in the turbulence intensity levels appears to have a two-gradient behaviour for all the results: an initial area of fast decay immediately downstream of the nozzle ($0 < x/D_H < 1$), followed by an area of slow decay where the turbulence values tend to gradually converge to a stable value. Moreover, the results also suggest that the bar diameter, d, significantly influences the amplitude and the decay rate of the turbulence intensity. This is evident as the grids with the same diameters generate a similar level of turbulence intensity and TI results exhibit a similar decay trend (A1 and A2, B1 and B2, C1 and C2), irrespective of the solidity ratio (σ). The turbulence intensity levels generated by grids A1, A2, B1, B2, C1, and C2 reach a plateau by $x/D_H = 1.25$ and have a constant value from this point downstream. These results are consistent with the literature [21]. Furthermore, apparent from the results in Fig. 6a, the grids at location A generate the highest turbulence intensity at the contraction nozzle outlet, compared to the results of grids at locations B and C. However, the turbulence intensity results also exhibit the highest turbulence intensity decay rate at this location. Turbulence intensities generated by grids at location A suffer approximately 40% reduction within the first hydraulic diameter.

The turbulence intensity results are previously presented in Fig. 6 for the distance downstream of the nozzle. However, in aerodynamic studies it is often presented by distance non-dimensionalized by grid geometry [21, 24]. Figure 7 presents the turbulence intensity decay results against the downstream distance, non-dimensionalized by grid bar diameter, d, (Fig. 7a) and grid mesh size, M (Fig. 7b). Figure 7 demonstrates the turbulence intensity decay of each grid and highlights that all grids lie on the same curve of decay, with the exception of A3 and A4. In corroboration with the results of Re_λ (Fig. 5, the highest rate of decay is observed for all grids within $0 < M < 20$.

2. Turbulence Integral Length Scale

The level of noise generated by a body immersed in a turbulent flow is not only dictated by the turbulence intensity level of the oncoming flow but also, among other quantities, by the size of the turbulent structures that interact with the body. In order to study the effect of the grid type and its location within the contraction nozzle on the size of the turbulent structures, the integral length scale (Λ_x) is estimated for all the grids employed in this investigation. The results are presented as the downstream evolution of the Λ_x, over a distance $1.6D_H$ from the nozzle exit, consistent with Fig. 6. In literature, there are multiple methods for estimating the integral length scale of the turbulent structures within the flow. In this study, Λ_x was estimated by using the autocorrelation method [37], where the stream-wise velocity autocorrelation function, i.e., Eq. 2, is employed. The curve fitting method using the Von-Kármán spectrum for isotropic turbulence [38] and the power spectrum method [39] were considered and comparable trends were observed, however, the results are not included for brevity. The normalized autocorrelation function of the velocity fluctuation u is defined as,

$$R_{uu}(\tau) = \frac{\overline{u(t)u(t+\tau)}}{u'^2}, \tag{2}$$

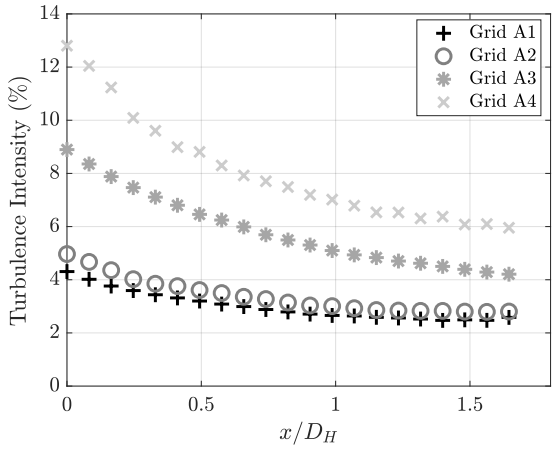

(a)

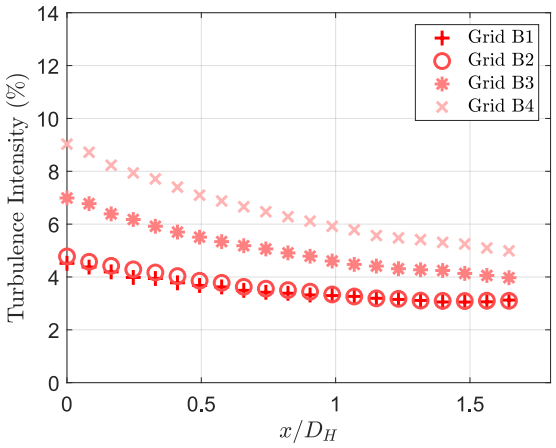

(b)

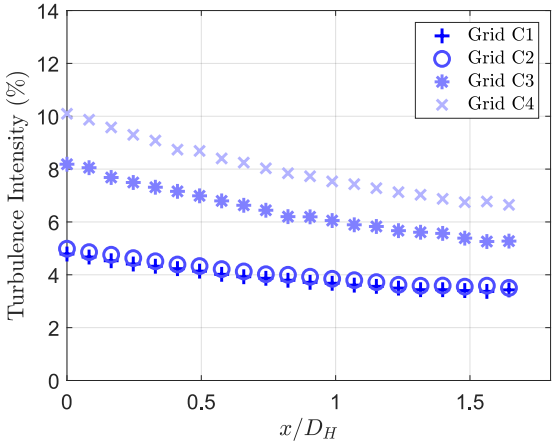

(c)

Fig. 6 Downstream evolution of the turbulence intensity from the nozzle exit ($x/D_H = 0$) for flow fields generated by grids at a) location A ($R = 1.3$), b) location B ($R = 2.4$), c) location C ($R = 4.4$), for a free-stream velocity $U_\infty = 20m/s$.

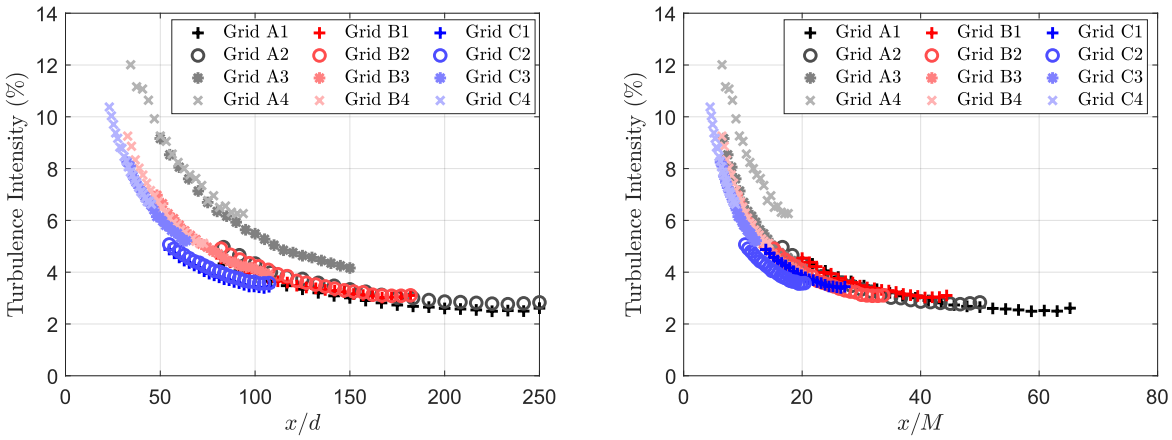

Fig. 7 Downstream evolution of turbulence intensity non-dimensionalized by grid geometry, for (a) non-dimensionalized by grid diameter (x/d) and (b) non-dimensionalized by grid mesh size (x/M).

where τ is the time-delay, and the overbar represents time-averaging. The integral of the autocorrelation function is defined as the integral time scale of the turbulence structures within the flow. Using Taylor's frozen turbulence hypothesis [40], and assuming the time-delay and stream-wise separation of the turbulent structures to be interchangeable, a simple multiplication between the free-stream velocity and the integral time scale provides the integral length scale of the turbulence structures in the stream-wise direction. The integral length scale is defined as,

$$\Lambda_x = U_\infty \int_0^\infty R_{uu}(\tau) d\tau. \tag{3}$$

The estimated integral length scales generated by all 12 turbulence grids are grouped with respect to their location in the contraction nozzle, and are presented for $0 < x/D_H < 1.65$ in Fig. 8. To ease the interpretation of the results, trend curves are added for the results of each case. Overall, the integral length scale increases with the downstream distance for all the presented cases and is consistent with literature [21, 24, 26]. The results at each location clearly demonstrate that the smallest bar diameter, as expected, generates the smallest integral length scale at the contraction nozzle outlet. Furthermore, as two grids at each location share the same bar diameter, i.e. A1 and A2, B1 and B2, and C1 and C2, the results indicate the grids generate comparable length scales at the contraction nozzle outlet. Moreover, considering the broader range of change in the integral length scale results (Λ_x) among grids A1, A2, A3 and A4 (Fig 8a), compared to the results for grids installed at locations B (Fig 8b) and C (Fig 8c), one may conclude that Λ_x is most susceptible to variations in the grid geometry at location A. These observations may suggest that diameter has an increasing influence on integral length scale at lower contraction ratio values. The analysis of flow anisotropy may indicate if the bar diameter sensitivity is influenced by the re-distribution of energy into the transverse components of turbulence due to the larger contraction ratio. This observation may have a particular importance for the open-jet

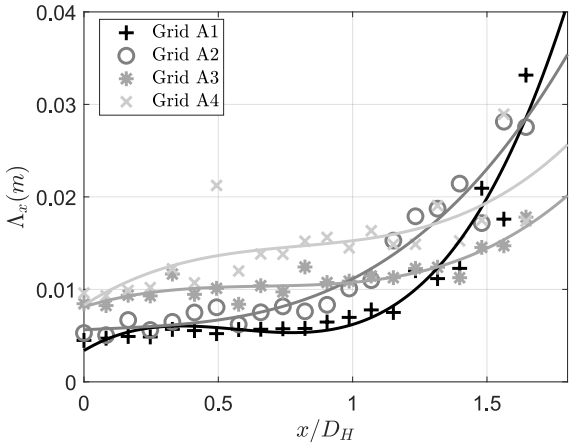

(a)

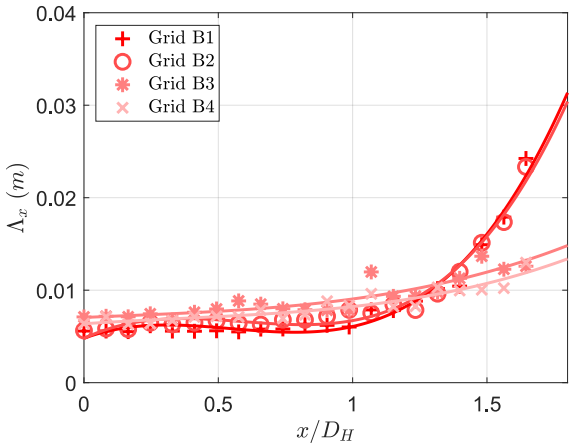

(b)

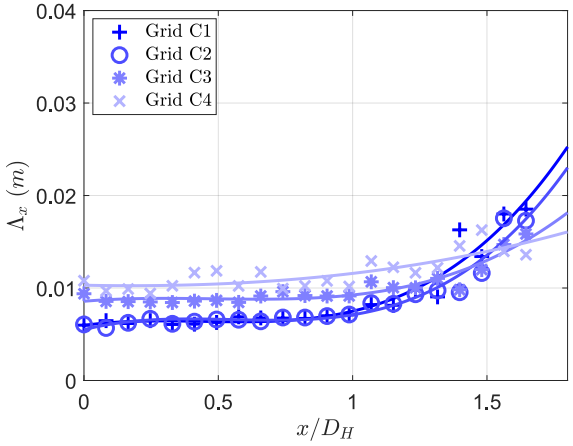

(c)

Fig. 8 Downstream evolution of the integral length scale, Λ_x, from the nozzle exit ($x/D_H = 0$), estimated for flow fields generated by grids at (a) location A ($R = 1.3$), (b) location B ($R = 2.4$), and (c) location C ($R = 4.4$), for a free-stream velocity $U_\infty = 20m/s$.

aeroacoustic facilities, where test models are often placed within the potential core of the jet and has a limited range of space to meet the flow requirements.

A further interesting factor that emerged from the analysis of Fig. 8 is the downstream evolution of the integral length scale. Every tested grid exhibits a consistent, almost linear, growth of the value of Λ_x from the contraction nozzle outlet ($x/D_H = 0$) to approximately $x/D_H \approx 1.25$. At this point, there is a secondary rapid growth of the Λ_x which appears to be sensitive to the value of grid bar diameter, d, and subsequently grid contraction ratio R. In general, the increasing value of R lessens the rapid growth observed beyond $x/D_H \approx 1.25$, moreover at each grid location, increasing the value of bar diameter and mesh size appear to reduce the secondary rapid growth that the integral length scale exhibits beyond $x/D_H \approx 1.25$.

Considering the integral length scale results in Fig. 8 together with the turbulence intensity results in Fig. 6, an inverse relationship can be observed between the rapid growth in integral length scale and the decay of the turbulence intensity, downstream of $x/D_H \approx 1.25$. The results suggest that when the decay of the turbulence intensity plateaus beyond the first hydraulic diameter, the integral length scale rapidly grows. In closed section wind tunnels, the integral length scale growth generally follows a linear trend with distance downstream from the grid [21, 25, 26]. However, to the best of the authors' knowledge, there is a lack of studies addressing the turbulence generation in open jet configuration wind tunnels. These observations suggest the possibility of a link between the downstream development of turbulence intensity and integral length scale in open jet wind tunnel configurations. It is also worth mentioning the relation between the integral length scale of the turbulent structures and the grid geometry. Previous studies in closed test section wind tunnels have shown that in the vicinity of the grid, the scale of the turbulent structures are in a size comparable to the bar diameter [21, 24, 25], even with a small grid contraction (R= 1.3), as is with the case for the grids at location A for the present study. Interestingly, the results suggest that the increase in the grid contraction ratio (R) is not accompanied by an increase in the integral length scale. As previously mentioned, the mesh size and the bar diameter were scaled based on the contraction ratio for the grids at location B and C, relative to the grids at location A. The observed scale of the integral length scale does not appear to follow this increase.

3. Turbulence Anisotropy

This section presents the anisotropy results of the flow fields generated by different grids employed in the experiments. The data collected from both a single-wire probe and an x-wire probe were assessed to understand the downstream evolution of the flow. Moreover, the results obtained through both measurements are compared to underline some important aspects to be considered in open-jet anechoic wind tunnel experiments. Firstly, the skewness and the kurtosis results calculated from single-wire probe data are presented, following the literature [41]. Secondly, the PSD of the velocity fluctuation from the single-wire is assessed and compared to the Von Kármán spectrum for isotropic turbulence. Finally, the anisotropy of the turbulent flow is assessed which is obtained from x-wire probe data.

To understand and evaluate the effect of the grid contraction ratio on the generated turbulence, it is key to first establish whether the turbulence is in a freely-decaying state. It is generally considered that for grid generated turbulence in closed-section wind tunnels, the freely-decaying region is observed within ten mesh lengths downstream of the grid [41]. The high-order statistical values of skewness and kurtosis are considered in the literature as a measure of whether the turbulence is fully developed [41]. Figure 9 demonstrates the downstream evolution of the skewness of the velocity fluctuations, the third-moment statistics, obtained through single-wire probe measurements, as $S(u_S) = \overline{u_S^3}/\overline{u_S^2}^{3/2}$, and the kurtosis of the velocity fluctuations, the fourth-moment statistics, as $K(u_S) = \overline{u_S^4}/\overline{u_S^2}^2$. Note that the velocity obtained through single-wire measurements is for u and v, and denoted as, u_S, as the singlewire sensor is sensitive only to velocity perpendicular to the wire. In freely-decaying turbulence, the expected skewness and kurtosis values are $S(u_S) = 0$ and $K(u_S) = 3$, respectively, and indicates that the PDF of the fluctuations in the flow has a Gaussian distribution.

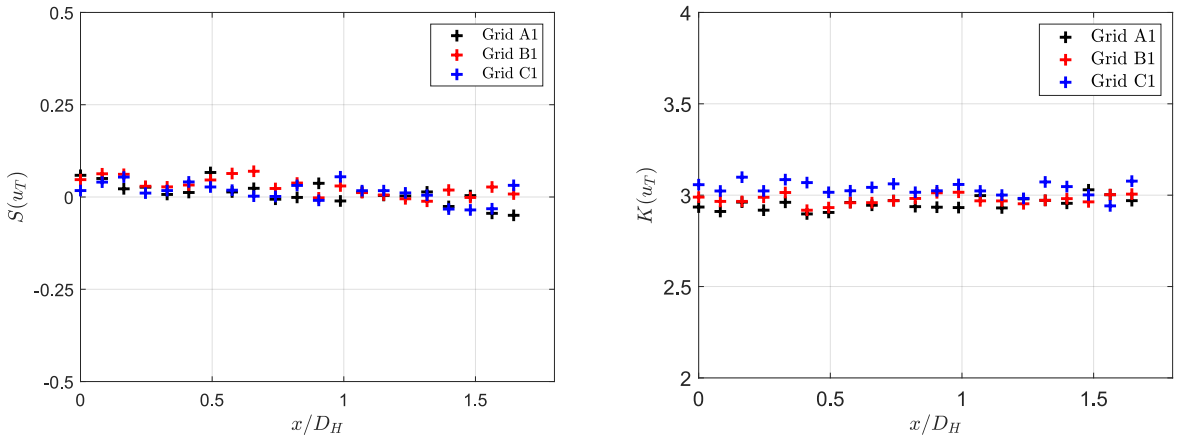

(a) **(b)**

Fig. 9 Downstream evolution of the (a) skewness, and (b) the kurtosis of the total velocity fluctuation (u_S) measured using a single-wire probe, from the contraction nozzle outlet $x/D_H = 0$ at a free-stream velocity of $U_\infty = 20$ m/s for turbulent flow generated by grids A1, B1 and C1.

Figure 9 shows the comparison of downstream evolution of the skewness factor (S) (Fig. 9a) and the kurtosis factor (Fig. 9b) for the velocity fluctuations generated by grids A1, B1 and C1 at $U_\infty = 20$ m/s within the measurement domain of $0 < x/D_H < 1.65$. Figure 9a shows the skewness value for the velocity fluctuations generated by all the grids is nearly zero across the full measurement domain, and there is only a slight departure from zero, indicating that the generated flow is in a state of freely-decaying turbulence for all the employed grids. Figure 9b displays the kurtosis factor which found to fluctuate around the nominal value of $K(u_S) = 3$, which indicates that the velocity fluctuations have a nearly Gaussian PDF distribution.

In aeroacoustic studies, it is common to evaluate the integral length scale of the flow structures from a single-wire hot-wire probe measurement by curve fitting to the Von Kármán spectrum for isotropic turbulence [38]. Generally, a

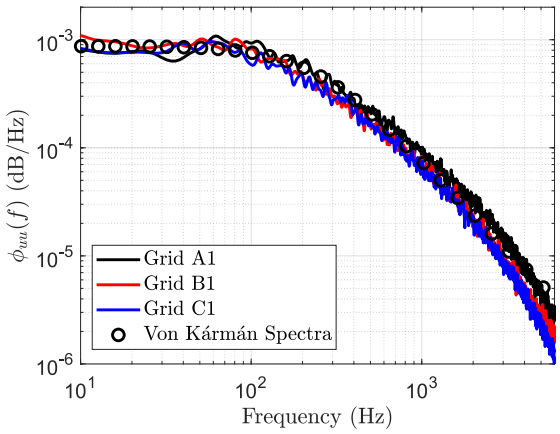

Fig. 10 Power spectral density of the velocity fluctuations (ϕ_{uu}) obtained from turbulent flows generated by grids A1, B1 and C1 measured at the contraction nozzle exit ($x/D_H = 0$), and the Von Kármán spectrum for isotropic turbulence fitted to Grid B1 results.

good fit of the power spectral density of the velocity fluctuations (ϕ_{uu}) against the Von Kármán spectrum is assumed as an indication that the incoming flow is isotropic [6, 14, 42–44]. Due to the limited number of aeroacoustic studies employing turbulence generating grids in open-jet wind tunnel facilities, the literature addressing the anisotropy (isotropy) levels, the method of defining anisotropy, and the downstream evolution of anisotropy is insufficient. The Von Kármán spectrum is defined as,

$$E(f) = \frac{4u'^2\Lambda_x}{U_\infty}\frac{1}{[1+(k_x/k_e)^2]^{5/6}}, \tag{4}$$

where

$$\frac{k_x}{k_e} = 2\sqrt{\pi}\frac{\Gamma(1/3)}{\Gamma(5/6)}\frac{f\Lambda_x}{U_\infty}, \tag{5}$$

k_x is the stream-wise wavenumber, k_e is the wavenumber range of energy-containing eddies, and Γ is a gamma function. Figure 10 demonstrates the energy spectrum of the velocity fluctuations generated by grids A1, B1, and C1, obtained from a single-wire probe measurement at the centre of the contraction nozzle outlet ($x/D_H = 0$) at the flow velocity of $U_\infty = 20$ m/s. For clarity, the Von Kármán curve fit is only plotted for the results obtained for grid B1 case. The integral length scale values estimated by Von Kármán curve fit for grids A1, B1 and C1 are $\Lambda_x = 0.013$ m, $\Lambda_x = 0.011$ m and $\Lambda_x = 0.010$ m, respectively. The values of integral length scale obtained from the Von Kármán fit method are higher, although of the same order of magnitude, than the results obtained through auto-correlation method (Section IV.A.2), which are reported in Table 2. The similar length scale values for the presented grids is likely due to the grid bar diameter (d) scaling with the grid contraction ratio (R).

On first inspection of Fig. 10, one can assume the flow is isotropic, following the method adopted in aeroacoustic literature. Despite the reasonable agreement observed between ϕ_{uu} and the Von Kármán spectrum for isotropic turbulence, the two-component velocity measurement can be used to assess the level of isotropy of the flow structures.

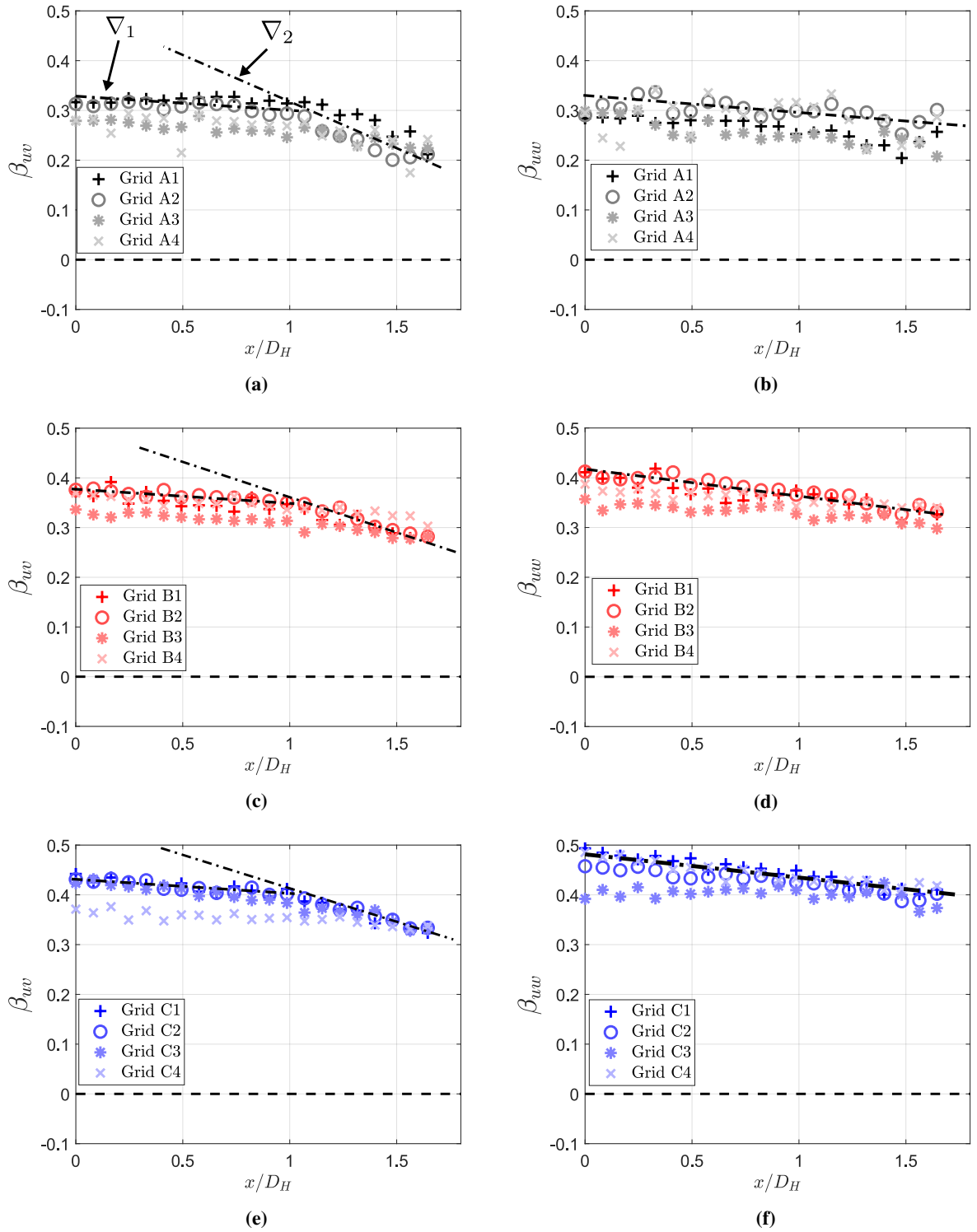

Fig. 11 Downstream evolution of the anisotropy of the transverse components of the flow from nozzle exit, $x/D_H = 0$. The left and right column presents the results for β_{uv} and β_{uw}, respectively, for cases employing the grids located at (a, b) A , (c, d) B, and (e, f) C , for a free-stream velocity $U_\infty = 20m/s$.

By using the root-mean-square velocity fluctuations, the anisotropy levels in the flow, can be estimated as,

$$\beta_{uv} = 1 - \frac{u'}{v'}, \quad \beta_{uw} = 1 - \frac{u'}{w'}. \tag{6}$$

In the case of isotropic turbulence u'=v'=w', leading to $\beta_{uv} = \beta_{uw} = 0$. Figure 11 presents the downstream evolution of the anisotropy levels for the turbulent flow fields generated by all the grids employed in this study. The anisotropy results obtained for the turbulence generated by the grids located at A, B and C are presented from top to bottom, respectively. Moreover, Figs. 11a, 11c and 11e present β_{uv}, and Figs. 11b, 11d and 11f present β_{uw}. Isotropic turbulence is expected to exhibit a value of $\beta = 0$ (u'=v'=w'), however previous experimental data have shown that deviations from zero may encompass a range of $-0.5 < \beta < 0$ and yet still be considered as isotropic due to the high level of uncertainty in hot-wire measurements of transverse velocity components (v and w) [21]. A negative value of β indicated a stronger fluctuation in the stream-wise direction.

Considering all of the results in Fig. 11, the following observations can be deduced. The results obtained from experiments employing different grid sizes, i.e. results from top to bottom, suggests that the anisotropy level of the grid turbulence deviates further from zero with an increase in the grid contraction ratio (R). Moreover, comparing the results of the anisotropy components, β_{uv} and β_{uw}, at each grid location, it is also evident that the anisotropy in turbulence differs between the two components of the velocity, v and w. In addition, as the contraction ratio increases, the difference between the magnitude of two anisotropy component, i.e., β_{uv} and β_{uw}, is exacerbated. Furthermore, the cross-wire probe measurement uncertainty does not account for the full deviation from isotropy across all the cases in addition to the trend of increasing R also leading to further deviation from isotropy. Finally, the downstream evolution of the results for all cases exhibit a slow decay towards isotropy. It is worth noting that the decay of the anisotropy values toward zero appears to have a two-gradient behaviour for the β_{uv} component. The β_{uv} results demonstrate a shallow gradient over $0 < x/D_H < 1$, followed by a steeper decay toward isotropy beyond $x/D_H > 1$. The spatial dependence of the anisotropy results are consistent with the trends observed for the turbulence intensity and integral length scale results (Figs. 6 and 8). However, the results for β_{uw} suggest a linear decay to isotropy with distance (x/D_H), but with a different decay rate compared to the results of β_{uv}.

Considering the turbulence anisotropy results, it is worth mentioning differences between turbulence generation in closed-section aerodynamic wind tunnels and open-jet aeroacoustic wind tunnels. The complex nature of the turbulence generation behind a grid and the straining of the developing turbulence structures through a contraction nozzle may affect the turbulence characteristics. For a typical closed test-section wind tunnel employed in aerodynamic measurements, the flow is constrained before being directed through a grid to generate isotropic turbulence [21]. To further improve the turbulence isotropy, a small secondary contraction is often employed at the grid downstream before the test section [24]. However, open-jet aeroacoustic facilities restrict the implementation of this methodology as the presence of the grids in

the contraction nozzle aims to reduce the self-noise of the grids. The large contraction following the grids could be a factor in the level of anisotropy presented here.

B. Far-field noise results

Having discussed the properties of the turbulence generated by the grids located at different locations in the contraction nozzle, this section of the paper addresses the far-field noise measurement results for the case studies. Moreover, this section evaluates the suitability of the grids to be employed in direct noise measurement setups for studies in open-jet aeroacoustic wind tunnel facilities. The far-field noise was measured using a polar microphone array located above the test models, as described in Section III. The measured noise results are presented in terms of the frequency-dependent energy content calculated for the pressure fluctuations measured by the microphones in the polar arc. The energy content is expressed in terms of dB/Hz, and is calculated as $10\log_{10}\left(\phi_{pp}/p_{ref}^2\right)$, where ϕ_{pp} is the power spectral density of the measured far-field pressure signal from the microphone, and $p_{ref} = 20\mu$Pa is the reference sound pressure. The power spectral density of the pressure fluctuations (ϕ_{pp}) was estimated by using the Welch's method [45], where the data from the transducers are segmented for 32 equal lengths with 50% overlap and windowed by the Hamming function, and the resulting spectrum had a frequency resolution of Δf =2 Hz. To ease the interpretation of the results and discussion, hereafter, $10\log_{10}\left(\phi_{pp}/p_{ref}^2\right)$ will be referred to as power spectral density (PSD). First, the results of the far-field noise generated by each grid is presented. This is followed by the results of the turbulence interaction noise studies with a NACA0012 airfoil and cylinder.

Figure 12 shows the background far-field noise measurement results for each grid at a free-stream velocity of U_∞ = 20 m/s. The presented results are obtained from the microphone located at a polar angle of 90°, as shown in Fig 4. Figure 12a displays the far-field noise results for the grids at location A (R = 1.3). This grid contraction ratio is cited as the optimum ratio for isotropic homogeneous turbulence generation in closed test-section wind tunnels [24]. However, comparing the background noise of the tunnel at U_∞ = 20 m/s (wind tunnel jet noise in the absence of grid, dashed line), to the self-noise generated by each grid at location A, it is evident that all the grids generate a significant level of self-noise. Notably, Grid A1 generates the highest levels of self-noise in comparison to grids A2, A3 and A4. In addition, the PSD results demonstrate that the difference in noise generated between each of the grids is, to some degree, similar above f = 500 Hz. The level of the grid self-noise is consistently in excess of the jet background noise (without grid). The far-field noise results for cases employing grids A1 and A2 share a common hump at around f = 1200 Hz, which corresponds to a common Strouhal number (St), as both grids have the same bar diameter. This observation may suggest that the hump in the far-field spectra at around 1200 Hz is caused by coherent shedding structures in the immediate wake of the grid which correspond to the size of the bar diameter.

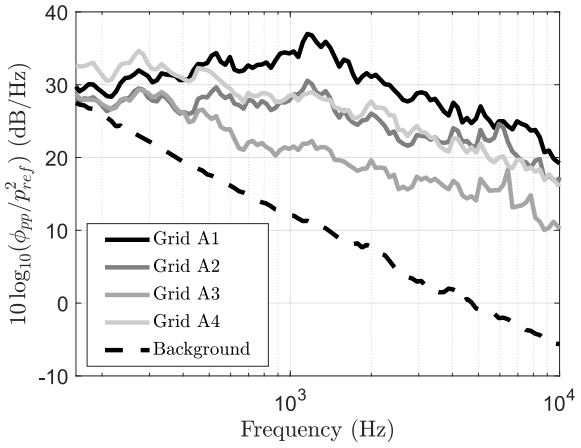

(a)

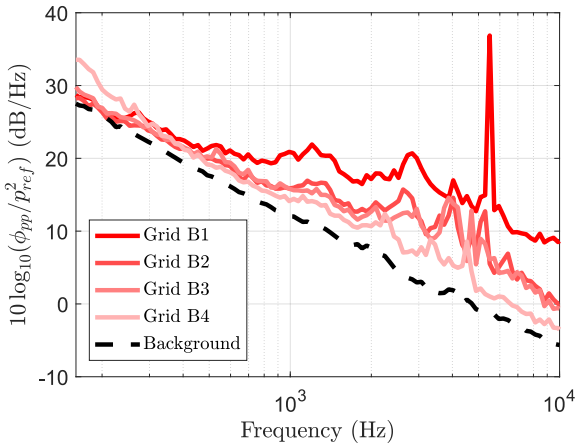

(b)

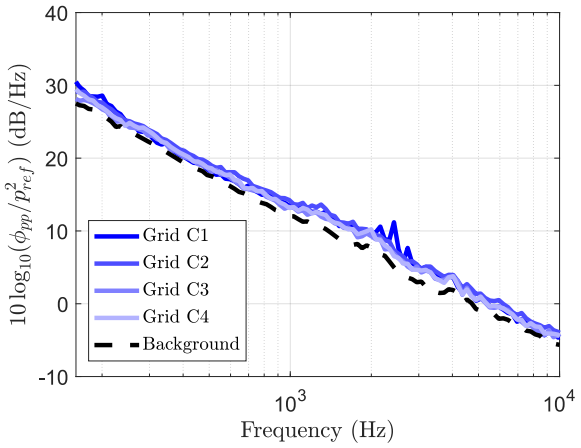

(c)

Fig. 12 Comparison of the far-field noise spectra generated by grids at a) location A ($R = 1.3$), b) location B ($R = 2.4$), c) location C ($R = 4.4$), and the background jet noise with no grid at $U_\infty = 20m/s$

Considering the geometric properties of the grids at location A (Table 2) together with the far-field measurement results, a potential causality between the solidity ratio of the grid (σ) and the far-field noise generation can be observed. The results show that Grid A1, which has the highest solidity ratio σ, generates the highest self-noise. Likewise, Grid A3 has the lowest solidity ratio σ, and generates the lowest levels of noise. The pressure drop across the grid is linked to the geometric property of σ, which is a factor in the self-noise generated by the grids the presented results in Fig. 12, consistent with the results in Geyer et al. [30].

Figure 12b presents the results of the self-noise generated by grids at location B ($R = 2.4$), in comparison to the normal background noise of the wind tunnel jet, at $U_\infty = 20$ m/s. The results for the grids mounted at location B display a reduction in the levels of the generated self-noise compared to the results of grids at location A. This may be due to the reduced velocity values at this upstream location in the contraction, where the flow interacts with the grid. Grid B1 has the highest solidity ratio, and across all measured frequencies, generates the highest level of far-field noise. It is worth noting that, unlike other grids, grid B1 generates a tone at around f=5500 Hz. This is believed to have been generated by flow leakage through the gaps created between the grid structure and contraction nozzle wall. Strouhal number analysis reveals a characteristic length much smaller than any grid geometry dimensions for fundamental shedding Strouhal number $St = 0.2$. The reason only B1 exhibits tonal behavior is likely due to the solidity. Grid B1 has a higher solidity than the other grids at location B, and thus generates a higher blockage and upstream pressure increase. For the results of the cases employing grids B2, B3, and B4, the average noise level generated above the jet background noise is significantly lower than the noise levels generated by Grid B1 and is less than 4 dB/Hz. At higher frequencies, above $f = 1000$ Hz, the results for the case employing grid B4 continues to follow the trend of the jet background noise. The average value of deviation from the background noise is less than 4 dB and peaks at around 10 dB/Hz. The results show that grids B2, B3 and B4 generate similar self-noise levels across the spectrum.

Figure 12c displays the self-noise generated by the grids at location C, which have the highest value of grid contraction ratio, i.e., $R = 4.4$. Considering the results for all cases (C1 to C4), it is apparent that these grids generate significantly lower levels of noise compared to grids located at A and B. The self-noise levels for all four grids are within 3 dB/Hz of the background noise level across the whole spectrum, except from a narrow band peak observed for grid C1 at approximately $f = 2400$ Hz. The grids at location C have a grid contraction ratio of $R = 4.4$, which suggests that the velocity at the proximity of the grid is significantly lower compared to the velocity values for grids at location A and B. The reduction in the velocity due to the increased contraction ratio is a significant contributor for the decreased levels of the grid self-noise. It is worth noting that, although the self-noise levels are within close proximity of the background noise level, the grid with highest solidity ratio (C1) seems to generate highest levels of self noise. These observations corroborate the link between the blockage created by the grid and generated self-noise reported by Geyer et al. [30].

Figure 13 shows the background far-field noise measurement results for grids A4, B4 and C4, compared with the no-grid jet background noise at three free-stream velocities of $U_\infty = 10$ m/s, $U_\infty = 15$ m/s, and $U_\infty = 20$ m/s. Figure

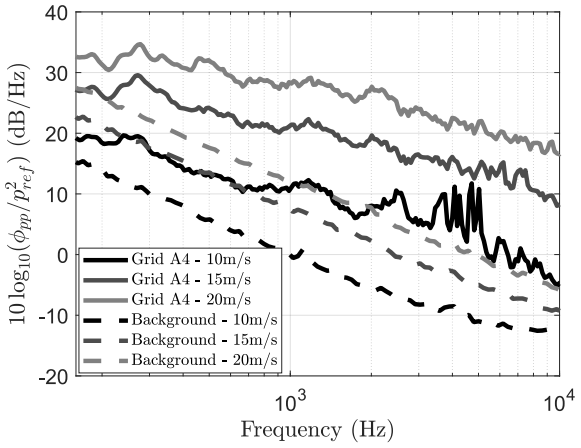

(a)

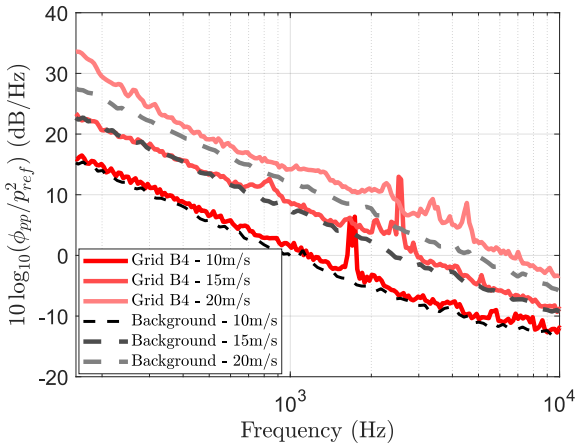

(b)

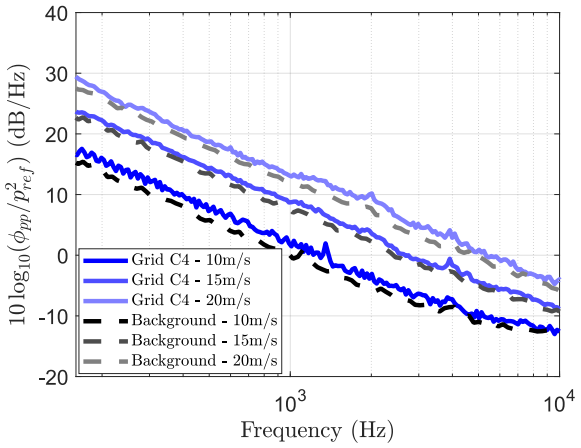

(c)

Fig. 13 Grid background noise dependency on velocity for $U_1 = 10$ m/s, $U_2 = 15$ m/s, and $U_3 = 20$ m/s for a) grid A4, b) grid B4, c) grid C4.

13a displays the far-field noise results for grid A4, at three velocities, measured by the microphone positioned at a polar angle of 90°. The background noise exhibits a systematic increase in noise across the presented frequency range as the velocity increases. The grid noise results for grid A4 in Fig. 13a show an increase with the velocity, similar to background noise spectrum. However, at lower speeds (U_∞ = 10 m/s) there appears to be an increase in the high frequency noise, in the form of discrete tones between 3000 Hz < f < 6000 Hz. The results indicate that a velocity increase reduces these tones at higher frequencies. Figure 13b shows that the self-noise of grid B4 exhibits tonal behaviour and at lower velocities the tones are more prominent. Figure 13c shows close agreement to the background noise as per Fig. 12, and displays that the dependency on velocity matches that of the background noise.

Following the discussions of the self-noise performance of each grid, the results for the far-field noise measurement in the context of turbulence interaction noise generation is presented. Figure 14 demonstrates the increase in noise generation due to the interaction of the NACA 0012 airfoil at $\alpha = 0°$ immersed in the turbulent flow generated by the grids under investigation. The results are presented in terms of the change in the levels of the far-field noise spectra relative to the grid self-noise spectra, $\Delta PSD = PSD_{NACA} - PSD_{grid}$. A positive ΔPSD refers to an increase in noise generation compared to the self-noise generated by the grid. Moreover, a significant increase with respect to the background noise may also indicate the possibility for direct (i.e., without the use of acoustic beamforming) and uncontaminated measurement of the interaction noise. Turbulence interaction noise is considered as a low-to-medium frequency mechanism [6], which suggests that the most pronounced deviations from the background noise (ΔPSD) are expected to be for lower frequencies.

Figure 14a demonstrates the magnitude of the noise increase due to the airfoil interaction with the turbulent flow generated by grids at location A, with respect to the self-noise generated by each grid. Recall that the grids at location A generate the highest levels of self-noise (see Fig. 12a). The ΔPSD results for all cases employing the grids at location A follow a similar trend across the whole spectra. At low frequencies (f < 200 Hz), the interaction noise is significantly higher than the grid self-noise for all cases (ΔPSD > 5 dB/Hz). Beyond f = 200 Hz, the ΔPSD steadily decreases for all cases up to f = 1000 Hz. Above f = 1000 Hz, the difference between the grid self-noise and the airfoil interaction noise is indiscernible. These observations suggest that direct noise measurements for interaction noise studies may be limited for f < 1000 Hz for the current setup. It is worth noting that Figure 14a demonstrates that grid A3, which generates the least self-noise among the grids at location A, leads to the highest excess noise relative to grid self-noise.

Figure 14b presents the difference between interaction noise generated by the NACA 0012 airfoil under the turbulent flow produced by the grids at location B and the self-noise of the corresponding grids (see Fig. 12b). Considering the results as a whole, a significant difference is evident compared to the results of the cases employing grids at location A, in Fig. 14a. The magnitude of the positive ΔPSD is elevated significantly, and the range of the ΔPSD is broadened. The ΔPSD display a minimum value of 6 dB/Hz over almost entire frequency range below f = 400 Hz. The highest level of ΔPSD is exhibited by the results of the case employing grid B4, which peaks at approximately f = 400 Hz and

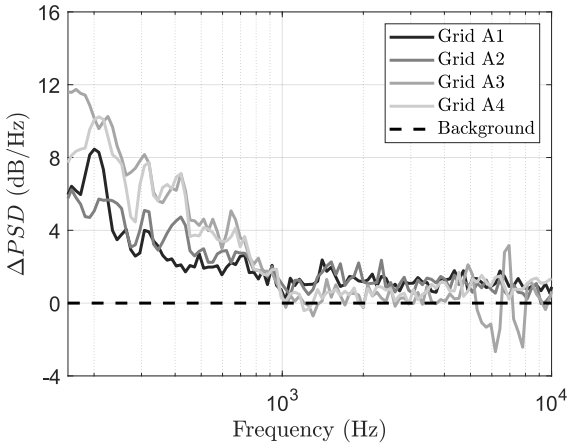

(a)

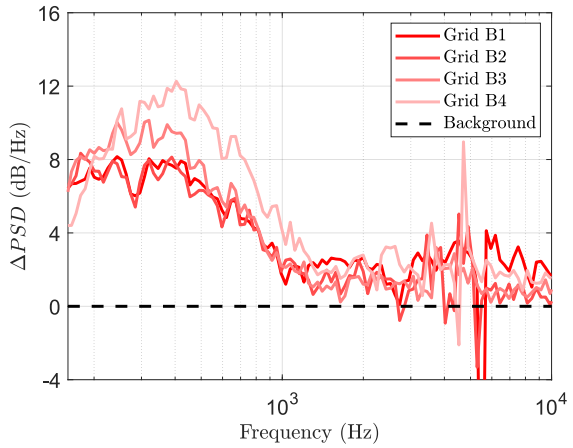

(b)

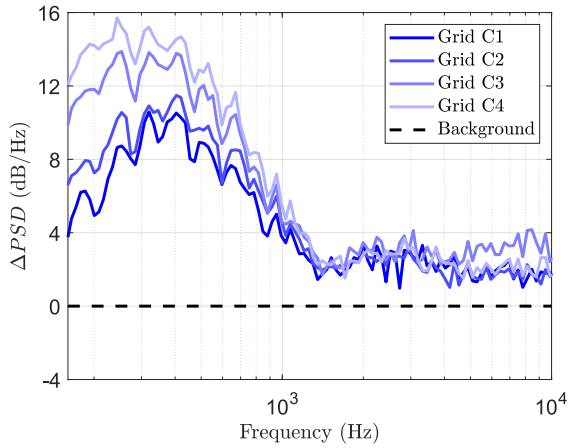

(c)

Fig. 14 Comparison of ΔPSD ($PSD_{NACA} - PSD_{grid}$) spectra at $\alpha = 0$ for turbulent flow conditions generated by grids at a) location A ($R = 1.3$), b) location B ($R = 2.4$), c) location C ($R = 4.4$) for a free-stream velocity $U_\infty = 20m/s$.

exhibits a difference of 12 dB/Hz compared to background noise. In addition, the apparent strong peaks and troughs at high frequencies are due to the strong tonal characteristics observed in grid self-noise results at high frequencies due to flow leakage. Another significant aspect to be underlined from Fig. 14b becomes apparent when the results are considered together with turbulence intensity results (Fig. 6). Although grids self-noise results do not show a significant difference at low frequencies, the results from the interaction noise study exhibits an apparent trend, where the ΔPSD results obtained from B1 and B2 cases collapse into a single curve. This trend is similar to the turbulence intensity results of the cases B1 and B2.

Figure 14c demonstrates the ΔPSD results for the interaction noise case study performed with the grids at location C. At low frequencies, the ΔPSD results display a similar trend to the results of the cases employing grids at location B. However, the ΔPSD values exhibit elevated magnitudes compared to the results of the grids with smaller R values, likely caused by the increased level of turbulence intensity in the results of the location C grids. The ΔPSD value peaks above 10 dB/Hz for all four grids at location C. The most pronounced difference between the self-noise and the interaction noise is exhibited by the cases employing grid C4 with a value of almost 16 dB/Hz. As the frequency increases, the ΔPSD spectra results of all cases collapse to a single curve. Moreover, above $f > 1000$ Hz, the ΔPSD values are consistently above the grid self-noise for the rest of the spectra. As indicated previously in the discussion of Fig. 14b, there exists a common trend between the ΔPSD spectra results for grids with similar turbulence intensity values. The results reaffirm the previous discussions that for the grids with a similar self-noise spectra, the grid that generate the higher turbulence intensity levels leads to the highest turbulence interaction noise.

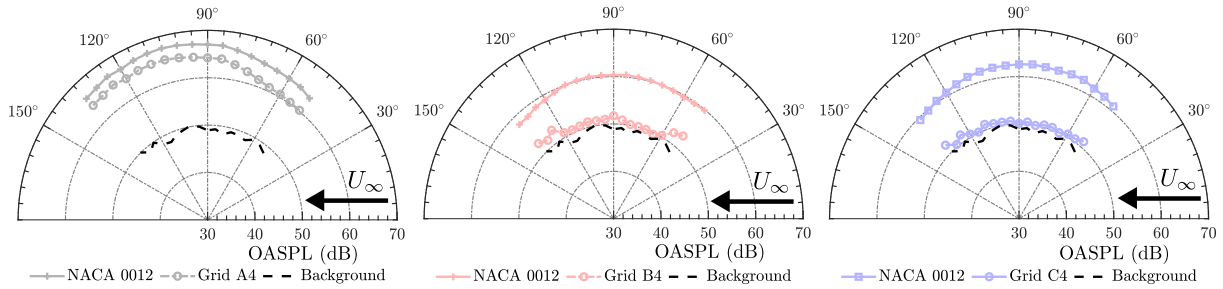

Fig. 15 Overall sound pressure level directivity results of the turbulence interaction study with a NACA0012 airfoil immersed in turbulent flow generated by grid a) A4, b) B4, and c) C4, in comparison with the normal background noise of the tunnel (no grid) and the grid self-noise at $U_\infty = 20$ m/s.

As was pointed out in the introduction of this paper, the main advantage of low-noise grids is to allow direct noise measurements. The implementation of the direct noise measurement technique is accompanied with the benefit of directivity measurements, which is practically not possible for the conventional acoustic beamforming techniques. Figure 15 presents the far-field directivity of the Overall Sound Pressure Level (OASPL) for the turbulence interaction case studies with the NACA 0012 airfoil. The results are presented for only representative cases for each contraction

ratio, namely the case studies performed with grids A4, B4 and C4. The non-weighted OASPL results are obtained for each microphone on the polar array by,

$$OASPL = 10\log_{10}\int(\frac{\phi_{pp}(f)}{p_{ref}^2})df. \tag{7}$$

The integration of the PSD data is carried out for a frequency range of 160 Hz and 10000 Hz. The polar angles refer to the microphone locations in the far-field microphone array (Fig. 4). Figure 15a shows the OASPL directivity results for the NACA0012 case study and the associated self-noise of grid A4. The jet background noise (no grid) is also provided for comparison. The results show that for all the microphones spanning the polar array, the OASPL of the grid self-noise is markedly higher than the normal background jet noise. The OASPL results indicate similar dipolar cardioid directivity pattern for both the grid self-noise and interaction noise. In addition, the noise level difference between the self-noise of grid A4 and the airfoil-interaction noise is consistently less than 3dB. Considering the results presented in Fig. 14a together with the OASPL results in Fig. 15a, one can conclude that the significant levels of the noise difference in ΔPSD results are completely hidden in the OASPL results. The OASPL results for the tests performed with the grid B4 show a significant reduction of self-noise compared to the OASPL results for grid A4. As seen, grid self-noise exceeds the no-grid jet background noise no more than 4 dB across the polar range of measurement. It is also worth noting that the directivity pattern of the OASPL results for this case demonstrates a monopolar-like behaviour. The OASPL results obtained from the experiments with the grid C4 in Fig. 15c reaffirms the previous observations, and show that the interaction noise level is consistently higher than both the background noise and the grid self-noise. Considering the results of cases with grid A4 and B4, the directivity patterns of the self-noise and the interaction noise demonstrate significant differences. However, for the case with grid C4, although the OASPL directivity of grid self-noise shows a monopolar behaviour, the interaction noise results show a dipolar cardioid pattern. The results of this investigation suggests that for aeroacoustic studies employing grid generated turbulence for open-jet wind tunnels, the directivity pattern of grid self-noise should carefully be examined.

A research topic which attracts much interest due to its broad application fields is the aerodynamics and aeroacoustics of cylinders exposed to turbulent flow. Hence, a case study involving cylinder-turbulent flow interaction is performed and the far-field noise results is presented. The cylinder was mounted to the same position as the NACA0012 airfoil (see Fig. 4), and the wind tunnel flow velocity was varied from 10 m/s to 25 m/s in increments of 5 m/s to understand the performance of the grid at a range of velocities. Based on the analysis and discussions provided earlier, a grid at location C, i.e., C2, is selected in order to demonstrate the effect of the free-stream velocity. Figure 16 presents the far-field noise measurement results generated by a cylinder immersed in the turbulent flow generated by grid C2 for free-stream velocities of 10 m/s $< U_\infty <$ 25 m/s. The figure shows the difference between the cylinder-turbulent flow interaction noise to grid self-noise at the associated velocity ($\Delta PSD(U_\infty) = PSD_{Cylinder}(U_\infty) - PSD_{grid}(U_\infty)$). The

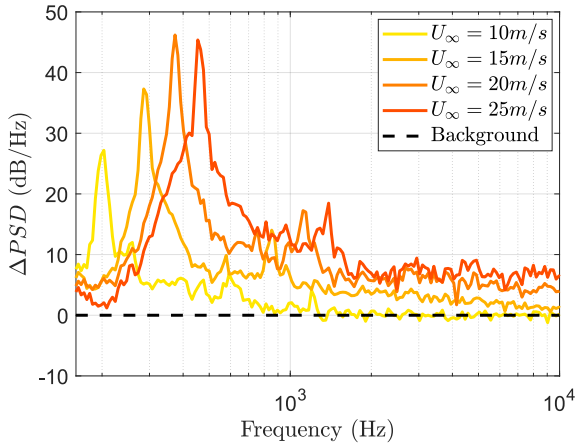

Fig. 16 Far-field noise spectra for the turbulence interaction noise generated by a cylinder immersed in the turbulent flow generated by grid C2 for the ΔPSD ($PSD_{cylinder} - PSD_{grid}$) spectra, at free-stream velocities of $10m/s < U_\infty < 25m/s$.

results demonstrate that increasing the free stream velocity increased both the level of noise generated by the cylinder in the turbulent flow and frequency of the tonal peak caused by vortex shedding, as expected. The magnitude of the tone in ΔPSD spectra increases with velocity up to U_∞ = 20 m/s. Beyond U_∞ = 20 m/s, the magnitude of the ΔPSD for the narrow band tone appears to be a constant. The tonal peaks in the results of Fig. 16 collapse to a common strouhal number of $St = 0.2$. The non-dimensionalized Strouhal number, $St = fD/U_\infty$, where f is the frequency, D is the cylinder diameter, and U_∞ is the free-stream velocity. The collapse of the peaks at $St = 0.2$ demonstrates the tonal noise due to the shedding in the wake of the cylinder. Further to this, Fig. 16 shows that with increasing free-stream velocity, the frequency range (width) of the tonal peak increases. This case study shows the ability of the grid C2 to deliver uncontaminated results for direct noise measurements for a range of velocities.

V. Conclusion

This paper presents the aeroacoustic analysis of a set of passive turbulence grids designed for an aeroacoustic open-jet wind tunnel. The main focus of the study was to identify and highlight the conditions for generating appropriate levels of turbulence, without compromising the ability to carry out direct measurements of the radiated far-field noise. The grids were passive grids and designed to operate in three stream-wise locations within the contraction nozzle. Each stream-wise grid location had four different turbulence grids, which had varied bar diameter values, d, mesh size, M, and subsequent solidity ratio, σ. In literature, grids with a contraction ratio of 1.3 are recommended for an ideal isotropic homogeneous turbulence production in closed test section wind tunnels [24]. However, considering the acoustic aspects for aeroacoustic studies, the self-noise generated with these grids dominates the spectra and renders direct noise measurement of any possible interaction noise study futile. Grids of a larger contraction ratio R = 2.4, offer a reduction in self-noise at frequencies less than f = 1000 Hz. However, the noise at higher frequencies was

littered with tones, which are likely caused by the geometry of the grids. The grids with the largest contraction ratio of $R = 4.4$, did not generate turbulence that was as close to isotropy as the smallest grids with a contraction ratio of $R = 1.3$. Nevertheless, it was possible to generate a turbulent inflow with comparable turbulence statistics (integral length scale and turbulence intensity), while only increasing the background noise by an additional 3 dB/Hz across the full spectra. The downstream evolution of the turbulence intensity and integral length scale is similar to that of a closed-section wind tunnel for the proximity of one hydraulic diameter. However, contrary to the trends observed in closed test-section results in the literature, beyond approximately one hydraulic diameter, the value of turbulence intensity tends to plateau, and the integral length scale demonstrates a rapid growth. Moreover, the anisotropy results suggest that the ability to fit the power spectral density of the velocity fluctuations obtained from a single-wire probe to the Von Kármán spectrum does not necessarily constitute evidence of isotropic turbulence for this investigation. The results underline the necessity for a thorough investigation of the anisotropy state of the turbulence with multi-component velocity measurements and a careful documentation for aeroacoustic tests performed in open-jet wind tunnel facilities. Moreover, the far-field measurement results show that direct far-field noise measurements with the least grid self-noise contamination are performed by employing a large contraction ratio between the grid and nozzle outlet area, with a compromise from the turbulence isotropy. Moreover, the grid self-noise OASPL directivity results suggest a thorough characterization of grid self-noise to enable correct interpretation of the turbulence interaction study results. Finally, the case studies results, performed with a NACA 0012 airfoil and cylinder, revealed that the grids that generated the least background noise tend to generate the highest interaction noise level.

Acknowledgments

The first author (L.B.) would like to acknowledge the financial support of Embraer S.A. and EPSRC (Engineering and Physical Sciences Research Council) via Grant No. EP/S013024/1 *"Aerodynamics and aeroacoustics of turbulent flows over and past permeable rough surfaces"*.

References

[1] Amiet, R., "Acoustic radiation from an airfoil in a turbulent stream," *Journal of Sound and Vibration*, Vol. 41, No. 4, 1975, pp. 407 – 420. https://doi.org/10.1016/S0022-460X(75)80105-2.

[2] Fink, M. R., "Experimental Evaluation of Theories for Trailing Edge and Incidence Fluctuation Noise," *AIAA Journal*, Vol. 13, No. 11, 1975, pp. 1472–1477. https://doi.org/10.2514/3.60559.

[3] Paterson, R., and Amiet, R., "Acoustic radiation and surface pressure characteristics of an airfoil due to incident turbulence," Proceedings of the 3rd Aeroacoustics Conference, Palo Alto, CA, AIAA-76-571, 1976. https://doi.org/10.2514/6.1976-571.

[4] Maryami, R., Showkat Ali, S. A., Azarpeyvand, M., and Afshari, A., "Turbulent flow interaction with a circular cylinder," *Physics of Fluids*, Vol. 32, No. 1, 2020, p. 015105. https://doi.org/10.1063/1.5119967.

[5] Devenport, W. J., Staubs, J. K., and Glegg, S. A., "Sound radiation from real airfoils in turbulence," *Journal of Sound and Vibration*, Vol. 329, No. 17, 2010, pp. 3470 – 3483. https://doi.org/10.1016/j.jsv.2010.02.022.

[6] Moreau, S., and Roger, M., "Effect of Angle of Attack and Airfoil Shape on Turbulence-Interaction Noise," 11th AIAA/CEAS Aeroacoustics Conference, Monterey, CA, AIAA-2005-2973, 2005. https://doi.org/10.2514/6.2005-2973.

[7] Hutcheson, F. V., Brooks, T. F., and Stead, D. J., "Measurement of the Noise Resulting from the Interaction of Turbulence with a Lifting Surface," *International Journal of Aeroacoustics*, Vol. 11, No. 5-6, 2012, pp. 675–700. https://doi.org/10.1260/1475-472X.11.5-6.675.

[8] Lyu, B., Azarpeyvand, M., and Sinayoko, S., "Noise Prediction for Serrated Leading-edges," 22nd AIAA/CEAS Aeroacoustics Conference, Lyon, France, AIAA-2016-2740, 2016. https://doi.org/10.2514/6.2016-2740.

[9] Lyu, B., and Azarpeyvand, M., "On the noise prediction for serrated leading edges," *Journal of Fluid Mechanics*, Vol. 826, 2017, p. 205–234. https://doi.org/10.1017/jfm.2017.429.

[10] Kim, J. W., Haeri, S., and Joseph, P. F., "On the reduction of aerofoil–turbulence interaction noise associated with wavy leading edges," *Journal of Fluid Mechanics*, Vol. 792, 2016, p. 526–552. https://doi.org/10.1017/jfm.2016.95.

[11] Narayanan, S., Chaitanya, P., Haeri, S., Joseph, P., Kim, J. W., and Polacsek, C., "Airfoil noise reductions through leading edge serrations," *Physics of Fluids*, Vol. 27, No. 2, 2015, p. 025109. https://doi.org/10.1063/1.4907798.

[12] Chaitanya, P., Joseph, P., Narayanan, S., Vanderwel, C., Turner, J., Kim, J. W., and Ganapathisubramani, B., "Performance and mechanism of sinusoidal leading edge serrations for the reduction of turbulence aerofoil interaction noise," *Journal of Fluid Mechanics*, Vol. 818, 2017, pp. 435–464. https://doi.org/10.1017/jfm.2017.141.

[13] Vemuri, S. S., Liu, X., Zang, B., and Azarpeyvand, M., "Leading-edge Serrations for Noise Control from Tandem Airfoil Configuration," 25th AIAA/CEAS Aeroacoustics Conference, Delft, the Netherlands, AIAA-2019-2556, 2019. https://doi.org/10.2514/6.2019-2556.

[14] Bampanis, G., Roger, M., Ragni, D., Avallone, F., and Teruna, C., "Airfoil-Turbulence Interaction Noise Source Identification and its Reduction by Means of Leading Edge Serrations," 25th AIAA/CEAS Aeroacoustics Conference, Delft, the Netherlands, AIAA-2019-2741, 2019. https://doi.org/10.2514/6.2019-2741.

[15] Celik, A., Mayer, Y. D., and Azarpeyvand, M., "On the aeroacoustic characterization of a robust trailing-edge serration," *Physics of Fluids*, Vol. 33, No. 7, 2021, p. 075120. https://doi.org/10.1063/5.0054767.

[16] Roger, M., Schram, C., and Santana, L. D., "Reduction of Airfoil Turbulence-Impingement Noise by Means of Leading-Edge Serrations and/or Porous Material," 19th AIAA/CEAS Aeroacoustics Conference, Berlin, Germany, AIAA-2013-2108, 2013. https://doi.org/10.2514/6.2013-2108.

[17] Geyer, T. F., Lucius, A., Schrödter, M., Schneider, M., and Sarradj, E., "Reduction of Turbulence Interaction Noise Through Airfoils With Perforated Leading Edges," *Acta Acustica united with Acustica*, Vol. 105, No. 1, 2019, pp. 109–122. https://doi.org/10.3813/AAA.919292.

[18] Geyer, T., Sarradj, E., Giesler, J., and Hobracht, M., "Experimental assessment of the noise generated at the leading edge of porous airfoils using microphone array techniques," 17th AIAA/CEAS Aeroacoustics Conference (32nd AIAA Aeroacoustics Conference), Portland, OR, AIAA-2011-2713, 2011. https://doi.org/10.2514/6.2011-2713.

[19] Bowen, L., Celik, A., Azarpeyvand, M., and da Silva, C. R. I., "On the use of Tailored Permeable Surfaces for Turbulence Interaction Noise Control," AIAA AVIATION 2020 FORUM- Virtual Event, AIAA-2020-2530, 2020. https://doi.org/10.2514/6.2020-2530.

[20] Simmons, L. F. G., Salter, C., and Taylor, G. I., "Experimental investigation and analysis of the velocity variations in turbulent flow," *Proceedings of the Royal Society of London. Series A, Containing Papers of a Mathematical and Physical Character*, Vol. 145, No. 854, 1934, pp. 212–234. https://doi.org/10.1098/rspa.1934.0091.

[21] Roach, P., "The generation of nearly isotropic turbulence by means of grids," *International Journal of Heat and Fluid Flow*, Vol. 8, No. 2, 1987, pp. 82 – 92. https://doi.org/10.1016/0142-727X(87)90001-4.

[22] Lavoie, P., Burattini, P., Djenidi, L., and Antonia, R. A., "Effect of initial conditions on decaying grid turbulence at low Rλ," *Experiments in Fluids*, Vol. 39, No. 5, 2005, pp. 865–874. https://doi.org/10.1007/s00348-005-0022-8.

[23] Uberoi, M. S., and Wallis, S., "Effect of Grid Geometry on Turbulence Decay," *Physics of Fluids*, Vol. 10, No. 6, 1967, pp. 1216–1224. https://doi.org/10.1063/1.1762265.

[24] Comte-Bellot, G., and Corrsin, S., "The use of a contraction to improve the isotropy of grid-generated turbulence," *Journal of Fluid Mechanics*, Vol. 25, No. 4, 1966, pp. 657–682. https://doi.org/10.1017/s0022112066000338.

[25] Batchelor, G. K., Townsend, A. A., and Taylor, G. I., "Decay of vorticity in isotropic turbulence," *Proceedings of the Royal Society of London. Series A. Mathematical and Physical Sciences*, Vol. 190, No. 1023, 1947, pp. 534–550. https://doi.org/10.1098/rspa.1947.0095.

[26] Kurian, T., and Fransson, J. H. M., "Grid-generated turbulence revisited," *Fluid Dynamics Research*, Vol. 41, No. 2, 2009, p. 021403. https://doi.org/10.1088/0169-5983/41/2/021403.

[27] Seoud, R. E., and Vassilicos, J. C., "Dissipation and decay of fractal-generated turbulence," *Physics of Fluids*, Vol. 19, No. 10, 2007, pp. 105–108. https://doi.org/10.1063/1.2795211.

[28] Cekli, H., and van de Water, W., "Tailoring turbulence with an active grid." *Experiments in Fluids*, , No. 49, 2010, pp. 409–416. https://doi.org/10.1007/s00348-009-0812-5.

[29] Paruchuri, C., Gill, J. R., Subramanian, N., Joseph, P., Vanderwel, C., Zhang, X., and Ganapathisubramani, B., "Aerofoil geometry effects on turbulence interaction noise," 21st AIAA/CEAS Aeroacoustics Conference, Dallas, TX, AIAA-2015-2830, 2015. https://doi.org/10.2514/6.2015-2830.

[30] Geyer, T., Poppe, W., and Sarradj, E., "Measurement of flow noise generation and pressure loss of nets and screens," *Applied Acoustics*, Vol. 134, 2018, pp. 69 – 74. https://doi.org/https://doi.org/10.1016/j.apacoust.2018.01.008.

[31] Mayer, Y. D., Jawahar, H. K., Szőke, M., Ali, S. A. S., and Azarpeyvand, M., "Design and performance of an aeroacoustic wind tunnel facility at the University of Bristol," *Applied Acoustics*, Vol. 155, 2019, pp. 358 – 370. https://doi.org/10.1016/j.apacoust.2019.06.005.

[32] Simmons, L. F. G., Salter, C., and Taylor, G. I., "Experimental investigation and analysis of the velocity variations in turbulent flow," *Proceedings of the Royal Society of London. Series A, Containing Papers of a Mathematical and Physical Character*, Vol. 145, No. 854, 1934, pp. 212–234. https://doi.org/10.1098/rspa.1934.0091.

[33] Devenport, W. J., Staubs, J. K., and Glegg, S. A., "Sound radiation from real airfoils in turbulence," *Journal of Sound and Vibration*, Vol. 329, No. 17, 2010, pp. 3470 – 3483. https://doi.org/10.1016/j.jsv.2010.02.022.

[34] Jørgensen, F., "How to measure turbulence with hot-wire anemometers - a practical guide," 2002.

[35] Schwarz, W. R., and Bradshaw, P., "Turbulence structural changes for a three-dimensional turbulent boundary layer in a 30° bend," *Journal of Fluid Mechanics*, Vol. 272, 1994, p. 183–210. https://doi.org/10.1017/S002211209400443X.

[36] Baidya, R., Philip, J., Hutchins, N., Monty, J., and Marusic, I., "Spanwise velocity statistics in high-Reynolds-number turbulent boundary layers," *Journal of Fluid Mechanics*, Vol. 913, 2021, p. A35. https://doi.org/10.1017/jfm.2020.1129.

[37] Atta, C. W. V., and Chen, W. Y., "Correlation measurements in grid turbulence using digital harmonic analysis," *Journal of Fluid Mechanics*, Vol. 34, No. 3, 1968, p. 497–515. https://doi.org/10.1017/S0022112068002041.

[38] von Kármán, T., "Progress in the Statistical Theory of Turbulence," *Proceedings of the National Academy of Sciences*, Vol. 34, No. 11, 1948, pp. 530–539. https://doi.org/10.1073/pnas.34.11.530.

[39] El-Gabry, L. A., Thurman, D. R., and Poinsatte, P. E., "Procedure for Determining Turbulence Length Scales Using Hotwire Anemometry," *Procedure for Determining Turbulence Length Scales Using Hotwire Anemometry*, 2014. https://doi.org/https://ntrs.nasa.gov/search.jsp?R=20150000733.

[40] Hinze, J., *Turbulence*, McGraw-Hill classic textbook reissue series, McGraw-Hill, 1975.

[41] Isaza, J., Salazar, R., and Warhaft, Z., "On grid-generated turbulence in the near- and far field regions," *Journal of Fluid Mechanics*, Vol. 753, 2014, p. 402–426. https://doi.org/10.1017/jfm.2014.375.

[42] Ayton, L. J., and Chaitanya, P., "An analytical and experimental investigation of aerofoil–turbulence interaction noise for plates with spanwise-varying leading edges," *Journal of Fluid Mechanics*, Vol. 865, 2019, p. 137–168. https://doi.org/10.1017/jfm.2019.78.

[43] Chaitanya, P., and Joseph, P., "Slitted leading edge profiles for the reduction of turbulence-aerofoil interaction noise," *The Journal of the Acoustical Society of America*, Vol. 143, No. 6, 2018, pp. 3494–3504. https://doi.org/10.1121/1.5040972.

[44] Bampanis, G., and Roger, M., "On the Turbulence-Impingement Noise of a NACA-12 Airfoil with Porous Inclusions," AIAA AVIATION 2020 FORUM- Virtual Event, AIAA-2020-2577, 2020. https://doi.org/10.2514/6.2020-2577.

[45] Welch, P., "The use of fast Fourier transform for the estimation of power spectra: A method based on time averaging over short, modified periodograms," *IEEE Transactions on Audio and Electroacoustics*, Vol. 15, No. 2, 1967, pp. 70–73. https://doi.org/10.1109/TAU.1967.1161901.